Article

Reductive Decomposition Kinetics and Thermodynamics That Govern the Design of Fluorinated Alkoxyaluminate/Borate Salts for Mg-Ion and Ca-Ion Batteries

Xiaowei Xie, Noel J. Leon, David W. Small, Evan Walter Clark Spotte-Smith, Chen Liao, and Kristin A. Persson*
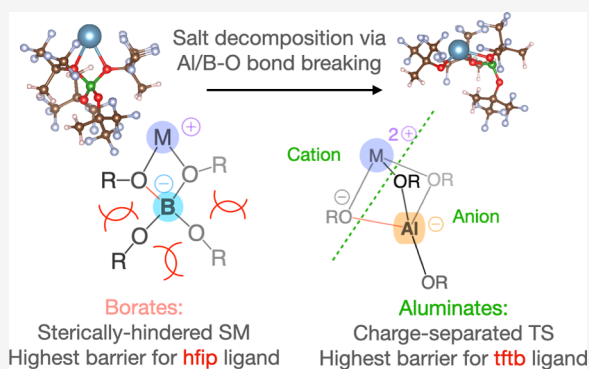
Read Online

ACCESS | 📊 Metrics & More | 📖 Article Recommendations | 🆂🆘 Supporting Information

ABSTRACT: The rational design of electrolytes has been a long-standing challenge in chemistry and materials science. In this work, we demonstrate a computational rationale for improving the performance of weakly coordinating electrolytes in currently challenging multivalent-ion battery applications, based on enhanced thermodynamic and kinetic stability against reductive decomposition. A series of fluorinated alkoxyborate and alkoxyaluminate salts are systematically examined based on their reduction and oxidation potentials and, motivated by NMR spectroscopy, detailed reductive decomposition pathways involving the breaking of Al/B−O, C−O, or C−F bonds are obtained. Based on the decomposition kinetics, the hexafluoro-*tert*-isopropoxy (hfip) ligand for borates and the trifluoro-*tert*-butoxy (tftb) ligand for aluminates are identified as promising ligands for constructing the salt anions. This borate prediction corroborates previous experimental work on $Mg[B(hfip)_4]_2$ and $Ca[B(hfip)_4]_2$, in which excellent electrochemical properties were reported. We find that steric factors govern the B−O bond-breaking decomposition kinetics while electronic factors are more important for aluminate salts. There is more charge transfer character in the aluminate transition states compared with borates for Al/B−O bond-breaking decomposition and thus electron-withdrawing ligands tend to stabilize the aluminate transition states. Such molecular-level understandings allow for better design principles for developing new electrolytes with improved stability and performance.

Salt decomposition via Al/B−O bond breaking

Cation
Anion

Borates:
Sterically-hindered SM
Highest barrier for hfip ligand

Aluminates:
Charge-separated TS
Highest barrier for tftb ligand

1. INTRODUCTION

Electrolyte design is a fundamental challenge in battery electrochemistry. Numerous interactions must be considered to optimize both the transport within the bulk electrolyte as well as interfacial reactivity. In the ideal case, an electrolyte should allow for reversible metal plating and stripping (if in contact with a pure metal electrode) or reversible intercalation and deintercalation (if in contact with an intercalation electrode) and should exhibit a wide electrochemical window. This stability can either be intrinsic or can be enabled by the formation of an appropriately passivating solid electrolyte interphase (SEI) layer. Most commonly, electrolytes are designed based on trial and error, guided by previous results for analogous systems; however, rational design based on computed electrolyte properties is a desirable alternative to accelerate the advancement of battery technologies. While Li-ion batteries remain dominant in applications ranging from electric vehicles to portable consumer electronics, multivalent batteries, such as Mg- or Ca-ion batteries, are receiving growing attention as next-generation alternatives.[1−3] However, to realize the promise of earth-abundant Mg or Ca energy

storage, improved understanding of the processes that govern electrolyte stability in these systems is needed.

As multivalent-ion systems tend to form more stable ion pairs in solution than their monovalent alkali metal ion counterparts,[4,5] metal ion de-solvation and undesirable metal ion-assisted anion decomposition reactions, especially from partially reduced metal ions such as Mg^+/Ca^+, present a formidable challenge. Theoretical investigations on magnesium bis(trifluoromethanesulfonyl)imide $(Mg(TFSI)_2)$ indicated that the ion pairs formed between partially reduced Mg^+ cations and $TFSI^-$ facilitate the decomposition of the anion through an energetically favorable C−S bond breaking.[6] It is also notable that simple salts for Mg-ion batteries, e.g., $Mg(TFSI)_2$ require a significant concentration of chloride
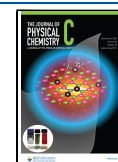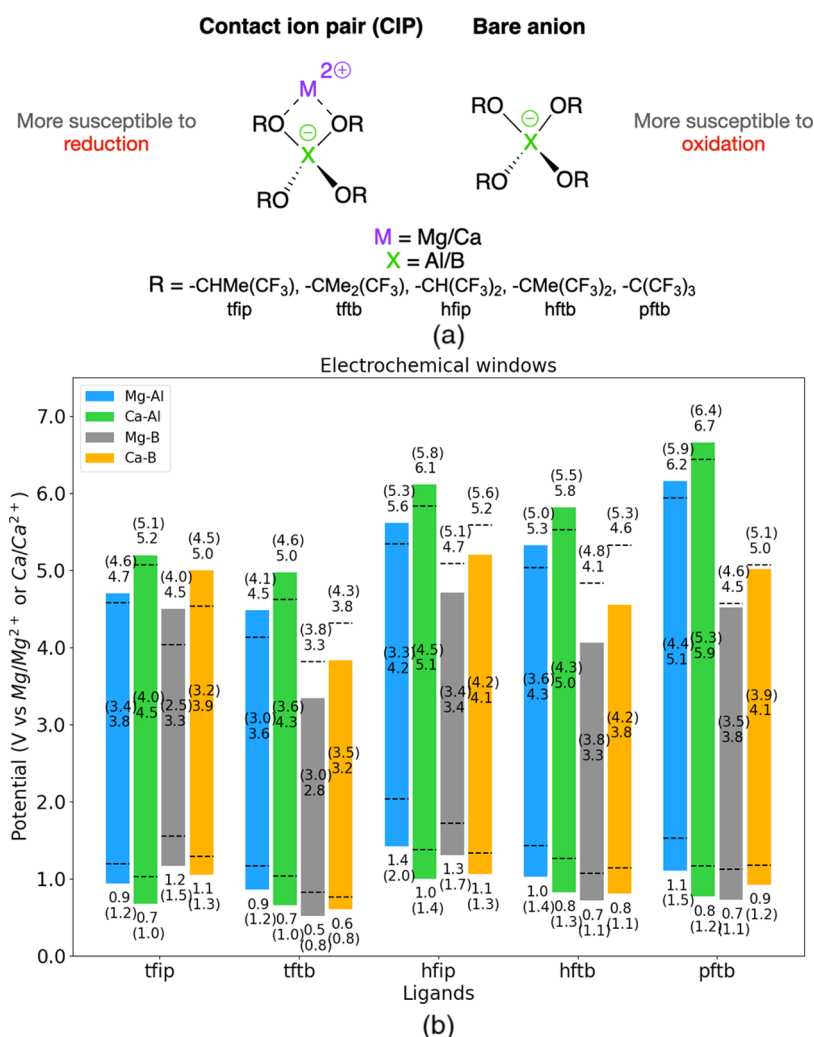
Figure 1. (a) Concept of contact ion pairs (CIP) and bare anions. (b) Electrochemical windows for the anions. Bare anions (X^- = monoanionic ligands) were used for oxidation potentials (upper limit) and contact ion pairs ($[M^{2+}X^-]^+$, M = Mg/Ca) were used for reduction potentials (bottom limit). Two levels of theory were used for comparison: the redox potentials shown in the regular bars are based on the ωB97X-D3/def2-TZVPPD/CPCM/RIJCOSX//ωB97X-D3/def2-SVPD/CPCM/RIJCOSX level of theory, whereas the black dashed lines and the numbers in parentheses are from the B3LYPD3BJ/def2-TZVPPD/CPCM//B3LYPD3BJ/def2-SVP/CPCM level of theory. The numbers in the middle of the bars are the energy gaps between the two redox potentials (stability windows).

(Cl^-) to enable plating/stripping at low overpotential.[7,8] Early investigations found that chloride (Cl^-) protects the passivation layer by oxidizing impurities like H_2O via the formation of Mg-Cl(ad) and/or $MgCl_2$.[8,9] More recently, cooperative anion effects between $TFSI^-$ and Cl^- have been observed in Mg-, Zn-, and Cu-based systems to enable more reversible metal dissolution and deposition, showcasing the importance of the relative association strength between the constituent anions and the working cations in tailoring the electrochemical performance of electrolytes.[10] In spite of their promise, chloride-based electrolytes are not compatible with high-voltage oxide cathode materials and usually suffer from corrosion problems, hindering practical applications of this strategy.

Recently, the fluorinated alkoxyaluminate/borate salts have emerged as a family of promising electrolyte candidates for Mg- and Ca-ion batteries.[11−17] Due to the presence of multiple electron-withdrawing fluorinated sites, the resulting anions tend to be weakly coordinating, leading to higher ionic conductivity and perhaps reducing the likelihood of undesirable Mg^+/Ca^+-assisted anion decomposition reactions.[6]

Following the initial success of one salt in this family, magnesium bis-tetrakis(hexafluoroisopropyloxy)borate (Mg[B-(hfip)$_4$]$_2$),[13,18,19] it was shown by Li[14] and Shyamsunder[15] that reversible Ca^{2+} deposition/stripping was possible at room temperature through the calcium version of this salt, Ca[B(hfip)$_4$]$_2$. In fact, based on both experimental and computational solvation structure analysis, the contact ion pair (CIP) population was found to be extremely low for Ca[B(hfip)$_4$]$_2$ in various ethereal solvents,[20,21] validating the design principle based on anion association strength.

Though initial electrochemical results show promise of fluorinated alkoxyborate and alkoxyaluminate salts, the structure−property relationships within this family of electrolytes remain unclear. In particular, insufficient attention has been paid to the electrochemical, thermodynamic, and kinetic stability of these salts. Along these lines of research, Jankowski et al.[22] reported free energies for decomposition reactions involving the breaking of B−O, C−O, and C−F bonds in a variety of Mg borate salts. They concluded that the delicate balance between the electron-withdrawing effects and the degree of ligand substitution in Mg[B(hfip)$_4$]$_2$ renders it the
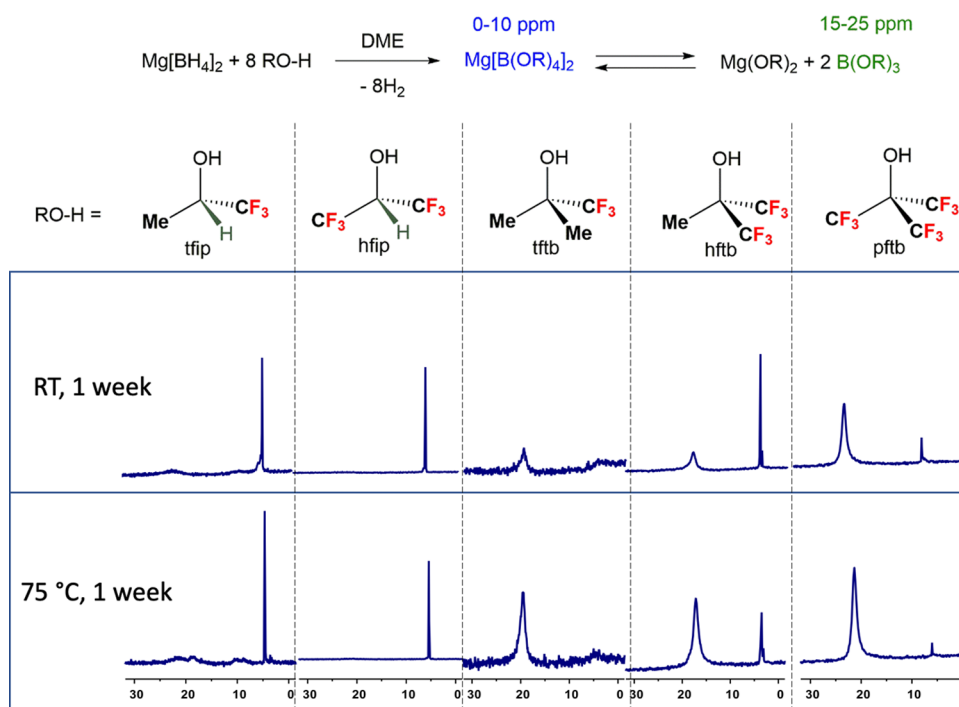
Figure 2. ^{11}B-NMR experiments on the Mg borate salts.

most promising Mg electrolyte. However, the complete decomposition pathways and the associated kinetic barriers were not addressed. Investigations of thermodynamic as well as kinetic stability are critical to ensure long cycling lifetimes. Although the CIP population can be constrained to be low by designing weakly coordinating anions, one can imagine that if there exist (thermodynamically and kinetically) favorable pathways for consuming the CIPs, the bulk equilibrium will restore the CIP population. Recently, we reported a Ca electrolyte, $Ca[TPFA]_2$, that is capable of room-temperature plating and stripping, and we found that the computed kinetic barriers for the reductive decompositions of $Mg[TPFA]_2$ and $Ca[TPFA]_2$ correlated well with an overall lower Coulomb efficiency of $Ca[TPFA]_2$ compared to $Mg[TPFA]_2$.[17] This hints at the possibility of discovering even more stable electrolytes via computational guidance.

In the present combined theoretical–experimental study, we systematically evaluate the redox stabilities for 10 fluorinated alkoxyaluminate/borate salts coupled with either Mg^{2+} or Ca^{2+} by examining their redox potentials and possible decomposition pathways through B/Al–O, C–O, and C–F bond cleavage. The alkoxy groups (as part of the anions) investigated here include the trifluoro-*tert*-isopropoxy (tfip = $-OCHMe(CF_3)$), trifluoro-*tert*-butoxy (tftb = $-OCMe_2(CF_3)$), hexafluoro-*tert*-isopropoxy (hfip = $-OCH(CF_3)_2$), hexafluoro-*tert*-butoxy (hftb = $-OCMe(CF_3)_2$), and perfluoro-*tert*-butoxy (pftb = $-OC(CF_3)_3$) groups. These abbreviations for these groups will be used throughout the remaining text.

We use kinetic barriers of reductive decomposition reactions as a metric for assessing and predicting electrolyte performance with respect to stability during cycling. Specifically, we argue that a high energy barrier for salt decomposition is desirable. Though it is possible for selective electrolyte degradation to positively contribute to electrode passivation and enable high Coulombic efficiency and capacity retention through SEI

formation, very few SEI layers in Mg-ion or Ca-ion batteries have possessed high ionic conductivity, often requiring high overpotentials to plate or strip.[7,23,24] One exception is when boron-hydrogen electrolytes are used, the formed SEI, consisting of boron clusters, does not negatively affect the Mg-ion transport.[25,26] $Mg[B(hfip)_4]_2$ is believed to form an SEI layer, and it exhibits superior electrochemical performance in Mg−S battery systems;[27] however, the functional properties of the film may not be sufficient without the addition of sacrificial additives in an Mg/Cu asymmetric cell.[28] Here, we suggest possible promising salts for both Mg-ion and Ca-ion batteries based on their computed properties. We further analyze the correlations between the decomposition barriers and the central element of the anions (Al vs B) and the alkoxy functional groups. These findings offer a path forward for deriving useful design principles for developing novel high-performance electrolytes.

2. RESULTS AND DISCUSSION

2.1. Electrochemical Windows. We calculate the theoretical electrochemical windows from the adiabatic ionization potentials (IP) and electron affinities (EA) for the anions, with and without the metal ion present. It has been shown that metal-coordinating anions (CIPs) are more susceptible to reduction than the bare anions, whereas the bare anions are more easily oxidized on the cathode.[16,29] Illustrative structures of CIPs and bare ions are outlined in Figure 1a. We show the computed electrochemical windows in Figure 1b, using the oxidation potentials for bare anions as the upper limit and the reduction potentials for CIPs as the lower limit. The complete electrochemical windows for CIPs and bare anions are given in SI Figures S1 and S2, respectively; we observe, as expected, that the electrochemical windows are consistently shifted upward when the metal ion (Mg^{2+} or Ca^{2+}) is present.
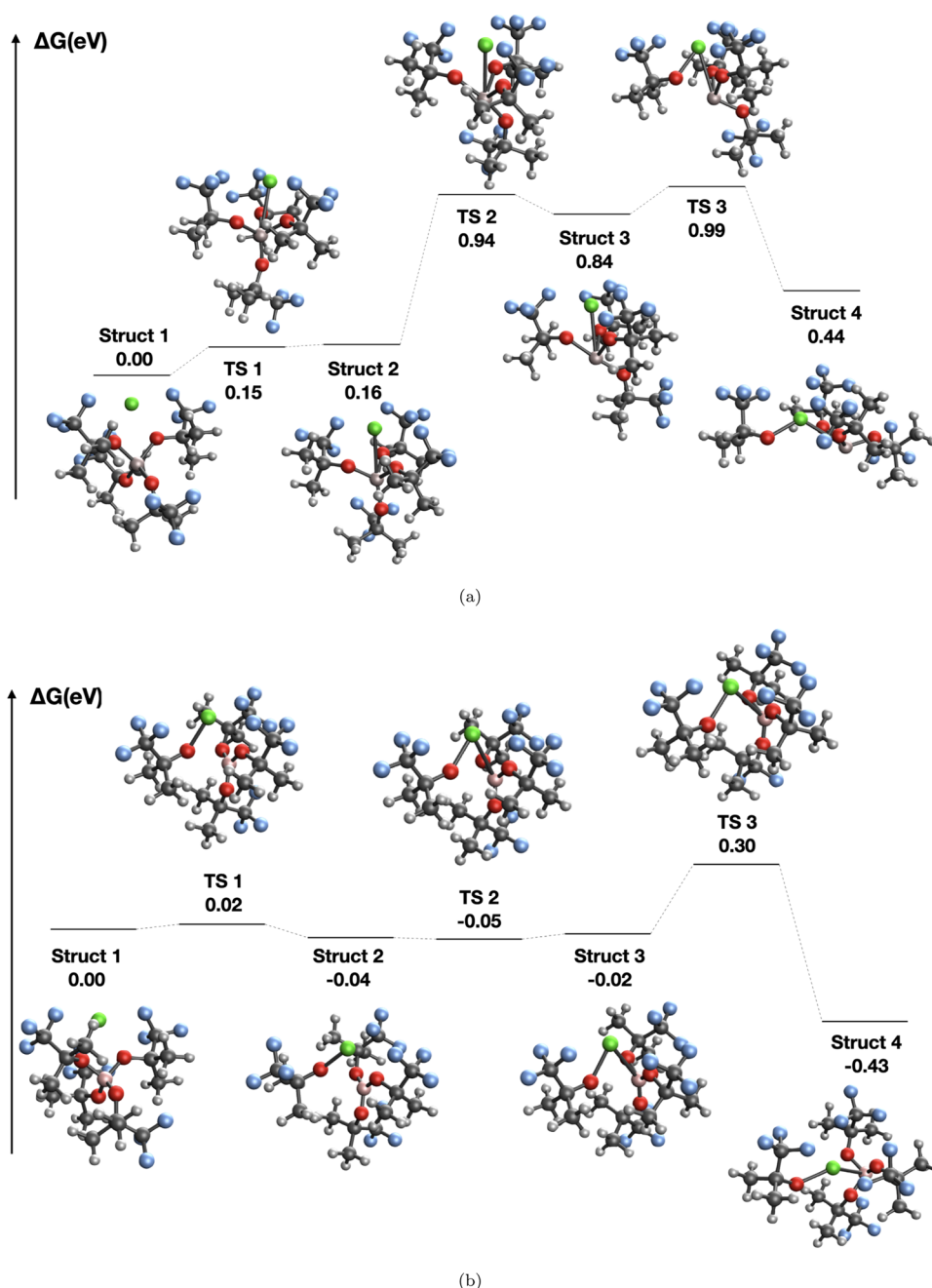
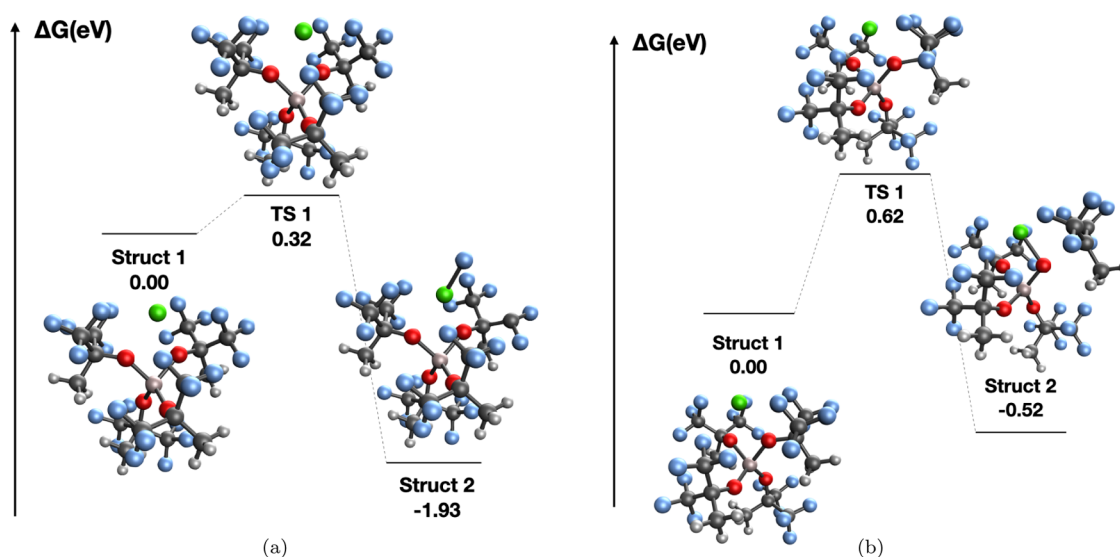**Figure 3.** Representative decomposition pathways through Al/B—O bond breakage: (a) $Ca^+[Al(tftb)_4]^-$ decomposition pathway and (b) $Ca^+[B(tftb)_4]^-$ decomposition pathway.

The oxidation potentials for the bare anions indicate great oxidative stability for all of the anions, although there exist some variations across the salts. The reduction potential of the CIP is a measure of how thermodynamically favorable reduction of the metal-coordinating anion is, at a certain potential. From Figure 1b, we find that all of the ion pairs show positive EAs at the Mg/Ca electrode potential, indicating they are all exergonic for single-electron reduction. It is worth noting that different levels of theory (B3LYP-D3(BJ)[30−32] vs ωB97X-D3)[33] result in fairly different absolute numbers, especially for the reduction potentials, which could differ by up to ~0.5 eV, but the trend across the different ligands remains. The differences between the two levels of theory in oxidation potentials for the bare anions mostly originate from

discrepancies in the optimal geometries for the two levels of theory (details given in SI Section I).

Across the ligands examined, we find that the tftb/hftb ligands have the potential to show relatively higher reductive stability while maintaining the weakly coordinating behavior. However, redox potentials alone do not determine performance, e.g., $Mg^+[B(HFIP)_4]^-$ shows relatively high reduction potential, yet it exhibits excellent electrochemical behavior experimentally.[13] High kinetic barriers for the subsequent decomposition reactions (after the initial one-electron reduction) can effectively inhibit detrimental decomposition, as has been hypothesized for the case of the acetonitrile (ACN) solvent in Mg systems.[34] In the following sections, we present a comprehensive investigation of reduction-mediated

Figure 4. Representative decomposition pathways through C−O and C−F bond breakage: (a) Ca$^+$[Al(hftb)$_4$]$^-$ decomposition through C−F bond breakage and (b) Ca$^+$[Al(hftb)$_4$]$^-$ decomposition through C−O bond breakage.

decomposition pathways, motivated by NMR spectroscopy, and elucidated by structure-chemical trends.

2.2. Decomposition of the Salts. *2.2.1. ^{11}B NMR Experiments.* To gain insight into the possible decomposition mechanisms of the salts, we conducted ^{11}B NMR experiments on the Mg borate salts in this family (Figure 2). Briefly, cooled solutions of Mg(BH$_4$)$_2$ in dimethoxyethane (DME) were reacted with its respective alcohol (ROH = tfip, hfip, tftb, hftb, and pftb), until no effervescence was observed. The reaction mixtures were heated mildly overnight to ensure complete conversion of borohydride starting material, as evidenced by the absence of doublets (0−20 ppm) in ^{11}B NMR spectra. Tfip is an exception as minor doublet signals were seen due to its low relative acidity. The mixtures were then left at either room temperature or 75 °C for 1 week and ^{11}B NMR spectra were recorded. All reactions were performed at approximately 0.1 M salt concentration in DME, a concentration chosen to provide the best solubility for Mg-anion products and to ensure a weak coordination environment for anions. For some cases (where ROH = tftb, hftb, and pftb), two unique peaks were observed, with characteristic signals corresponding to the anionic four-coordinate B (0−10 ppm) and the neutral three-coordinate B (15−25 ppm),[35−37] respectively. We note that it is difficult to monitor these reactions over time because the NMR samples cannot be sealed if they evolve gaseous byproducts (H$_2$). ^{11}B NMR spectra for the reaction mixture after stirring overnight were recorded (SI Figure S58); there is no significant change in the species present and the general trends remain the same. ^{19}F NMR was also conducted (SI Figures S59 and S60), but ^{19}F NMR spectra are less informative due to the relatively close signal of all of the −CF$_3$ groups, and the resulting difficulty in assigning signals as mixtures.

The presence of both tri-/tetra-coordinate boron species indicates a rearrangement of alkoxide ligand from the boron center to a magnesium cation, when the alkoxide is sterically bulky enough to overcrowd the tetra-coordinate boron center. At elevated temperatures, more B(OR)$_3$ is produced through B−O bond breaking for the tftb, hftb, and pftb ligands, accompanied by precipitation of solid byproducts and lowered signal-to-noise ratio in the spectra. Mg[B(OR)$_4$]$_2$ is stable at

75 °C when R = tfip/hfip. This result provides experimental evidence for B−O bond-breaking decomposition even without reducing conditions, which motivated us to investigate the Al/B−O bond decomposition further computationally.

2.2.2. Decomposition Barriers for the Neutral Ion Pairs. We examine three types of decomposition patterns for the one-electron reduced CIPs, namely, from breaking the bond that is closest to the metal ion in each of the following bond categories: (1) Al/B−O, (2) C−O, and (3) C−F. The Al/B−O bond breaking decomposition is discussed in Section 2.2.1, the C−O bond breaking decomposition was proposed in ref 16, and the C−F bond breaking decomposition is considered because MgF$_2$ and CaF$_2$ are observed in the SEI with this family of electrolytes.[15] Figure 3a,3b shows exemplary free energy diagrams for the Al/B−O bond breaking decomposition, i.e., for Ca$^+$[Al(tftb)$_4$]$^-$ and Ca$^+$[B(tftb)$_4$]$^-$. Figure 4a,4b shows free energy diagrams for examples of the C−O and C−F bond-breaking decompositions, i.e., for Ca$^+$[Al(tftb)$_4$]$^-$. A complete set of energy diagrams for other salt variations are given in the SI, for all combinations of M$^+$[X(Y)$_4$]$^-$ (M = Mg/Ca, X = Al/B, Y = tfip, tftb, hfip, hftb, and pftb); a simplified version (showing energy levels only) of those energy diagrams for Al/B−O bond breakage is shown in Figure 5a. We note that although all of the ligand variations exhibit qualitatively similar Al/B−O breaking decomposition pathways for aluminates and borates, they can differ in the number of reaction steps and intermediates; in such cases, in Figure 5a, we have aligned the horizontal positions of the energy levels for analogous structures across the series (e.g., where the degree of the Al−O/B−O bond dissociation matches, etc.). The rate-limiting step of a decomposition pathway is determined by the energy difference between the starting material (or the lowest-energy intermediate, if lower in energy than the starting material) and the highest-energy TS. The rate-limiting decomposition barriers for all considered bond breakages and ligand variations are given in Figure 5b. For the C−O bond-breaking paths, the rate-limiting barrier is shown in Figure 5b only when the barrier is less than 1.0 eV (see the discussions later in this section).
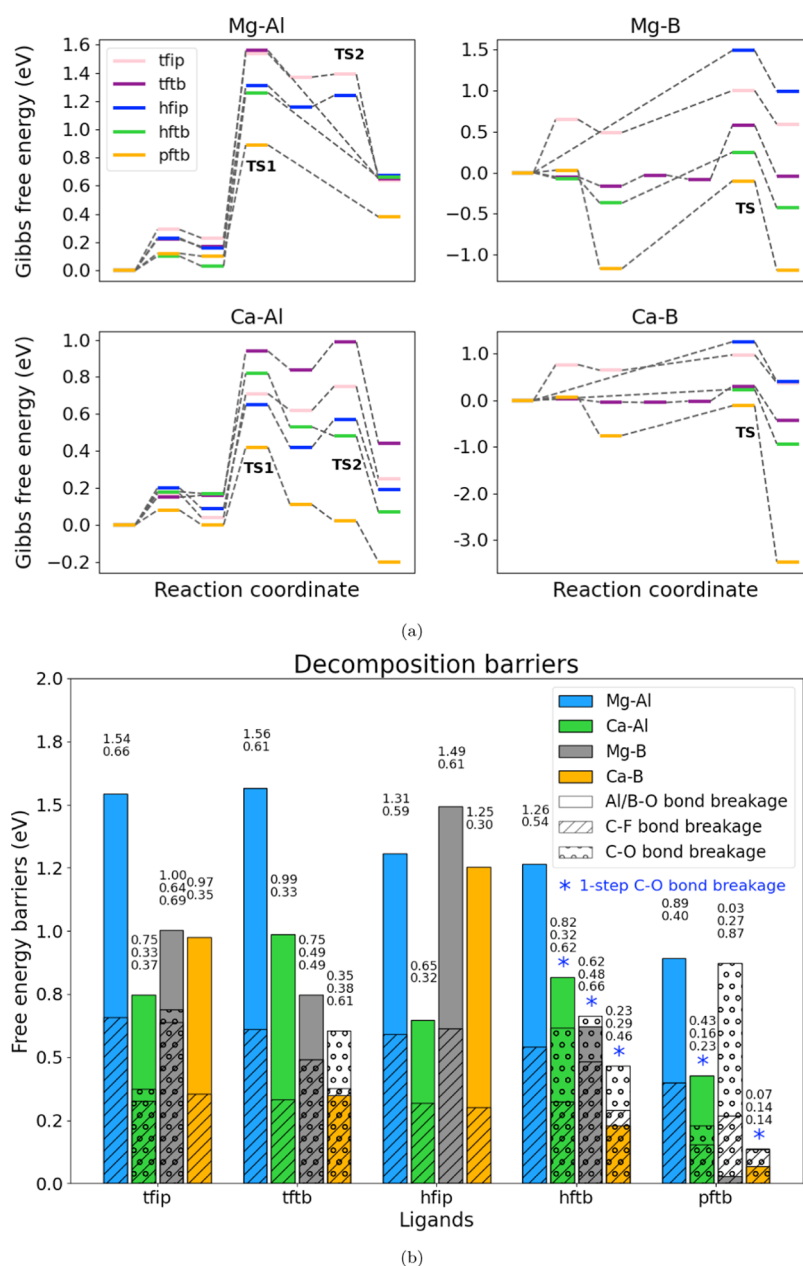
Figure 5. Decomposition pathways and rate-limiting barrier heights. (a) Decomposition pathways for Al−O/B−O bond breakage. (b) Rate-limiting decomposition free energy barriers for Al−O/B−O, C−F, and C−O bond breakage. The numbers on each bar from the top to bottom are the rate-limiting barriers for Al/B−O bond breakage, C−F bond breakage, and C−O bond breakage. Note that the C−O bond-breaking barrier is only shown when it is less than 1.0 eV.

To identify the origin of the differences in the energy profiles, we analyze the Al/B−O bond-breaking pathways from a structural perspective. In the case of the aluminates, taking $Ca^+[Al(tftb)_4]^-$ as an example (Figure 3a), the initial bidentate (Al coordinating to two oxygens in the anion) rearranges over a low barrier (0.15 eV) to a tridentate CIP (Struct 2), followed by a rotation of the axial Al−O bond (Struct 2 → TS2 → Struct 3). Subsequently, the Al−O bond opposite (180°) to the aforementioned rotated Al−O bond breaks to create the decomposed product, $Ca^{2+}(tftb)^-[Al(tftb)_3]^-$ (Struct 3 → TS 3 → Struct 4). The initial rotation of the Al−O bond exhibits low barriers for all of the ligand variations (<0.3 eV), consistent with the longer Al−O bonds (∼1.8 Å) compared with the B−O bonds (∼1.5 Å), which allows the aluminates to deviate more easily from the tetrahedral geometry, creating

space for an extra electron. For borates, on the contrary, we see a more straightforward dissociation of one B−O bond, although in some cases, such as for $Ca^+[B(tftb)_4]^-$, minor geometrical arrangement steps may precede the rate-limiting TS (TS 3) (Figure 3b). Unique among the borate salts are the complexes with the pftb ligand, where the B−O bond is already significantly dissociated at the intermediate geometries: see Struct 2 in Figure S17 for $Mg^+[B(pftb)_4]^-$, where the B−O bond is 3.52 Å and Struct 2 in Figure S22 for $Ca^+[B(pftb)_4]^-$, where the dissociated B−O bond is 4.05 Å. These dissociation lengths are reached before the principle TS, i.e., the one that is qualitatively conserved across all ligands and labeled as "TS" in Figure 5a. Thus, we consider the TS before those intermediates (TS1 in Figures S17 and S22) the rate-limiting TS with very low barriers of 0.03 and 0.07 eV, respectively.
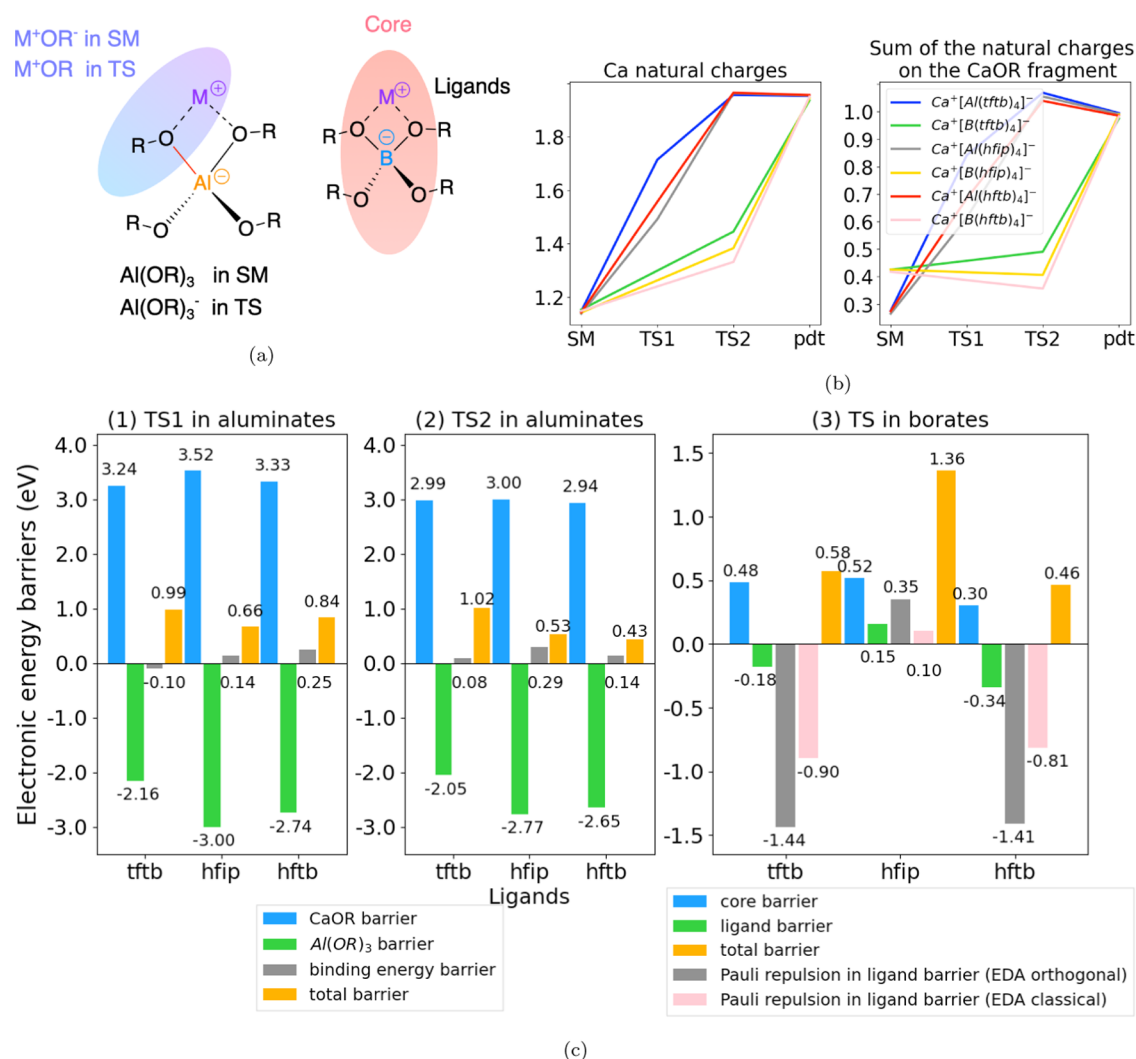
Figure 6. Al/B−O bond-breaking barrier analysis for aluminates/borates. (a) Illustrative picture of how the complexes are divided into two regions for probing the origin of the barrier differences. (b) Natural charge analysis for the Ca and the CaOR (OR = tftb, hfip, and hftb) fragment. (c) Electronic energy barriers for different fragments. (1) The electronic energy barriers for the CaOR and the $Al(OR)_3$ fragments for the TS1 geometry (see Figure 4a). Note that different total charges are used for the SM and TS in computing the barriers for each fragment. The CaOR barriers are calculated from the $[CaOR]^0 \rightarrow [CaOR]^+$ transition; the $Al(OR)_3$ barriers are calculated from the $[Al(OR)_3]^0 \rightarrow [Al(OR)_3]^-$ transition. Similarly, the binding energy barriers correspond to subtracting the binding energy between $[CaOR]^0 - [Al(OR)_3]^0$ in the SM from the binding energy between $[CaOR]^+ - [Al(OR)_3]^-$ in the TS. The CaOR barrier, the $Al(OR)_3$ barrier, and the binding energy barrier sum to the total energy barrier; (2) is the same as (1) but is for the TS2 geometry in aluminates. (3) Barriers for the borates calculated with the core part of the ligand part taken from the original SM and TS geometries. Note that for the core part, H atoms are added to the O atoms and for the ligand part, H atoms are added to the C atoms that were previously bound to O atoms. The positions of these Hs were optimized with the coordinates of all other atoms fixed.

Comparing the full energy diagrams across the ligand variations shown in Figure 5a and the rate-limiting barriers shown in Figure 5b, we note that the tftb ligand exhibits the highest barrier for decomposition across aluminate salts, whereas the hfip ligand exhibits the highest barrier across borate salts, regardless of whether Mg^+ or Ca^+ is the counter ion. Experimentally, there has been remarkable success with the $[B(hfip)_4]^-$ anion, in both Mg[13] and Ca[14,15] systems, consistent with the high decomposition barriers observed in our calculations. Specifically, the $Mg[B(hfip)_4]_2$ salt has shown exceptional electrochemical performance in terms of oxidative stability (~4 V vs Mg), ionic conductivity, and coulombic efficiency.[13] Some instabilities of the $Mg[B(hfip)_4]_2$-based electrolytes against the magnesium metal were observed for long-term cycling; however, it was due to the reductive decomposition of the solvent triglyme (G3) but not the $[B(hfip)_4]^-$ anion, as evidenced by the auger electron spectroscopy (AES) and X-ray photoelectron spectroscopy (XPS) spectra.[38] The $Ca[B(hfip)_4]_2$ salt also supports reversible Ca^{2+} deposition/stripping, although the accumulation of CaF_2 on the Ca surface indicates reductive salt instability.[15] For aluminates, there are some experimental investigations on the Mg salts while the Ca version of the salts are less reported on. $Mg[Al(hfip)_4]_2$ demonstrated excellent coulombic efficiency,[11,12] and $Mg[Al(pftb)_4]_2$ showed oxidative and reductive stability;[16] they are predicted from our calculations to possess decomposition barriers of 1.31 and 0.89 eV, respectively. As the Ca salts (ion pairs) trend toward lower barriers than their Mg counterparts, we predict their performance will be the most affected by the specific ligand

choice. For instance, our calculations indicate that the tftb ligand needs to overcome a 0.99 eV barrier to decompose, whereas the pftb ligand only needs to overcome a 0.43 eV barrier; the difference in these numbers implies a significant difference in rate constants for decomposition at room temperature. We note that the barriers may not necessarily correspond quantitatively with the experimental rate constants, as density functional theory (DFT) limitations and effects such as explicit solvation and solvent rearrangement are unaccounted for here; however, the predicted qualitative trend can be employed to guide the comparison between the ligand variations.

Examining the C−F bond-breaking decomposition pathways, all variations of salts exhibit a straightforward one-step path for Ca$^+$ to abstract a fluorine atom from the −CF$_3$ group in the nearby alkoxy group. In Figure 4a, we show one example of such a path, i.e., for Ca$^+$[Al(hftb)$_4$]$^-$, which showcases a low barrier of 0.32 eV. As shown in Figure 5b (and the energy diagrams in SI Section IV), such fluorine-abstracting decomposition pathways are highly exergonic ($\Delta G \sim -2.0$ eV) with low barriers for all salt variations (the largest barrier is 0.66 eV for Mg$^+$[Al(tfip)$_4$]$^-$). Our calculations also indicate that the Ca salt barriers generally trend lower than their Mg counterparts, consistent with experimental observations that increased CaF$_2$ formation on the anode surface, compared to MgF$_2$.[15] Although low barriers and large negative reaction ΔG's are observed here, we note that the first coordination sphere of the metal ion is saturated with solvents, e.g., Mg^{2+} is sixfold coordinated by oxygen atoms from both solvent molecules and the salt anions for Mg(TFSI)$_2$ in diglyme,[39] and this aspect is missed in our calculations. We also speculate that mitigating reactions such as hydrogen abstraction may provide avenues to restore the salt efficacy in this case, in contrast to, e.g., the more detrimental Al/B−O bond-breaking reactions, which will likely cause an irreversible salt breakdown.

Finally, a single-step C−O bond-breaking decomposition pathway was identified for some salt variations, mainly Ca salts with the hftb or pftb ligands (Ca$^+$[Al(hftb)$_4$]$^-$, Ca$^+$[Al(pftb)$_4$]$^-$, Ca$^+$[B(hftb)$_4$]$^-$, Ca$^+$[B(pftb)$_4$]$^-$, and Mg$^+$[B(hftb)$_4$]$^-$, see bars labeled with blue stars in Figure 5b, and the complete energy diagrams are given in SI Section III). For borates, a B−O bond would break simultaneously with the C−O bond breaking, consistent with observations by Jankowski et al.[22] For single TS reactions, the barriers for C−O bond breaking decomposition are comparable in magnitude (usually very low) to that for Al/B−O bond decomposition. Hence, C−O bond-mediated decomposition is expected to manifest for these salts. For the other salts, a multistep path involving the product from C−F bond breakage was identified, possessing a high rate-limiting barrier due to a stable intermediate state (see SI Section III). Nevertheless, we have included the rate-limiting barriers in Figure 5b if they are less than 1.0 eV.

Considering the kinetic barriers for all types of decomposition pathways, we identified the tftb ligand as the most promising ligand for aluminate salts because it exhibits the highest barrier for decomposition under reductive conditions, whereas the hfip ligand shows the most promise in the borate salt series, for both Mg and Ca systems.

2.3. DFT Investigation of the Difference in Decomposition Kinetics between Aluminates and Borates.

DFT-based analysis was undertaken to elucidate the apparent differences in the kinetic barriers across the ligand variations

for the borate/aluminate salts, i.e., the high barrier of the tftb (hfip) ligand for aluminates (borates), respectively.

We divided the ion pair complexes into different structural components to qualitatively isolate the substructure that is responsible for the barrier variations. In the current investigation, we performed two kinds of division, as shown in Figure 6a. The aluminum ion pair complexes were divided into the M−OR (M = Ca/Mg) and the Al(OR)$_3$ substructures (Figure 6a: left); the boron ion pair complexes were divided into the core (B,O, and Ca/Mg) and the ligands (Figure 6a: right). In the following section, for simplicity, we focus on the Ca salts with the following three ligands (tftb, hfip, hftb) for investigation of the barrier differences. We consider these three examples to be representative, as they occur in the middle of the electronegativity/bulkiness range of the five ligands. We note the conclusions obtained here can be extended to the tfip and pftb ligands as well as the Mg version of these salts.

We analyzed the charge distribution across these complexes for both the starting material (SM) and the TS geometries, based on the natural atomic charges obtained from the natural bond orbital (NBO) analysis.[40] In Figure 6b, we plot the change in natural charge for the Ca atom (on the left) and the change in the sum of the natural charges on the CaOR fragment (on the right) for the SM, TS, and product geometries. Note that the set of aluminate rate-limiting TSs, i.e., one for each ligand variant, comprises two distinct structure types, corresponding to "TS1" and "TS2" on the energy diagram shown in Figure 5a. However, there is only one rate-limiting TS structure type for the borates (plotted as "TS" in Figure 5a or "TS2" in Figure 6b). As the reaction proceeds, the Ca oxidation state changes from Ca$^+$ to Ca^{2+}, which is expected and aligns well with previous studies.[6] The Ca natural charges for the borates at the TSs are significantly smaller than those for the aluminates (both TS1 and TS2), indicating that the aluminate TSs show more charge-separated character. This is also reflected in the sum of natural charges on the CaOR fragments: the aluminate TSs are close to [CaOR]$^+$ [Al(OR)$_3$]$^-$ in character, while the CaOR components in borate TSs are approximately neutral. The amount of charge transfer can also be deduced from plotting the isosurface of the spin density, which is more well defined than the atomic partial charges as there are numerous possible definitions of the latter. The spin density plots are shown in SI Figures S52−S57. To further elucidate why the aluminate TS exhibits an enhanced charge transfer character, we calculated the EAs for Al(OR)$_3$ and B(OR)$_3$. In SI Section VII, we show three types of such values, namely, the adiabatic electron affinity (EA), vertical attachment energy (VAE), and vertical detachment energy (VDE), the latter two representing the vertical electron affinities at the optimized neutral and anion geometries, respectively.[41] An apparent distinction between B(OR)$_3$ and Al(OR)$_3$ (see Figure S51) is that all of the B(OR)$_3$ compounds show negative adiabatic EAs, whereas the Al(OR)$_3$ EAs are positive, indicating the B(OR)$_3$ compounds are less amenable to reduction. Even in the case of the optimal anion geometries (bent), the VDEs for B(OR)$_3$ present more than 1 eV lower than their Al(OR)$_3$ counterparts. Even though full charge transfer must be reached in the end product, the borate salts evolve through neutral B(OR)$_3$, which lowers the energy. This phenomenon can be indeed observed from the energy diagrams: e.g., in Figure 3b the BO$_3$ moieties are close to planar (as is optimal for isolated neutral B(OR)$_3$) for all TS geometries, whereas for aluminates, the AlO$_3$ moieties are

Table 1. Selected Parameters ((the Laplacian of the Density $\nabla^2\rho$, Density at the Bond Critical Point ρ @BCP(3,-1), Mayer Bond Order m, Bader Atomic Charges q) for the QTAIM Analysis of the Starting Complexes)

structure	bond path	bond length (Å)	$\nabla^2\rho$ (a.u.) @BCP(3,−1)	ρ (a.u.) @BCP(3,−1)	m	q(Al/B), q(O)
Ca$^+$[Al(tftb)$_4$]$^-$	Al−O	1.802	0.602	0.075	0.584	2.553, −1.373
Ca$^+$[Al(hfip)$_4$]$^-$	Al−O	1.803	0.599	0.074	0.578	2.566, −1.365
Ca$^+$[Al(hftb)$_4$]$^-$	Al−O	1.798	0.608	0.075	0.592	2.565, −1.363
Ca$^+$[B(tftb)$_4$]$^-$	B-O	1.540	0.445	0.126	0.715	2.369, −1.312
Ca$^+$[B(hfip)$_4$]$^-$	B−O	1.506	0.548	0.138	0.765	2.369, −1.320
Ca$^+$[B(hftb)$_4$]$^-$	B−O	1.568	0.378	0.116	0.671	2.378, −1.305

easily bent (i.e., tetrahedral-like, which is optimal for isolated anionic Al(OR)$_3$) from early on (Figure 3a).

The joint analysis of the bonding structure of the SMs (the CIPs) by the quantum theory of atoms in molecules (QTAIM[42]) and the more qualitative noncovalent interaction (NCI) plot[43,44] method reveals the covalent and noncovalent nature of the Al−O and B−O bonds. Table 1 lists the information extracted from the QTAIM study, i.e., electron density values ρ and values of the laplacian of the density $\nabla^2\rho$ at bond critical points (BCPs, i.e., (3,−1)-type points),[42] and from the analysis of the corresponding Bader atomic charges q and Mayer bond orders m. The electron density at the BCP indicates the amount of shared density between the bonded atoms, and the Laplacian of the electron density depicts the extent of charge concentration or depletion.[42,45] The fact that the ρ values at the critical points are of the magnitude of 7×10^{-2} (for aluminates) and 1×10^{-1} (for borates) and that the $\nabla^2\rho$ values are larger than zero indicate the Al−O and B−O bonds in the starting tetrahedral ion pairs are both in the ionic regime,[46] with B−O being more covalent in character.

To further visualize the types of interactions involved in the Al−O or B−O bonding, we employed the NCI plot method, which utilizes the reduced density gradient as an indicator of noncovalent interactions, as characterized by large density gradients in the regions where the density itself is small. The type of NCI can be further classified by the sign of the second eigenvalue λ_2 of the Hessian of ρ, i.e., stabilizing and bonding-like interactions are present when $\lambda_2 < 0$, destabilizing or repulsive interactions when $\lambda_2 > 0$, and finally dispersion interactions when λ_2 is close to 0. These regions can be conveniently visualized from the blue, red, and green colors, respectively, on an NCI plot. Figure 7 shows NCI plots for the Ca$^+$[Al(hfip)$_4$]$^-$ and Ca$^+$[B(hfip)$_4$]$^-$ complexes, where in the case of Ca$^+$[Al(tftb)$_4$]$^-$, an attractive NCI isosurface is clearly present in between the Al−O bonds, whereas the NCI isosurface of Ca$^+$[B(tftb)$_4$]$^-$ is repulsive, corroborating the more ionic nature of the Al−O bond vs B−O bond. The blue attractive region is enlarged in the TS2 for Ca$^+$[Al(tftb)$_4$]$^-$ compared with the SM, mostly likely due to the increased favorable electrostatic interactions from the charge separation as discussed earlier.

We reiterate that even at TS1, the amount of charge transfer in the aluminates is significantly larger than for the borates, as reflected in both the Ca natural charges and the spin density plots shown in SI Figures S52−S57. The results indicate that almost an entire electron is transferred from Ca$^+$ to the Al(OR)$_3$ component at the stage of the TS (regardless of whether it is TS1 or TS2). To estimate the electronic contribution of the CaOR and Al(OR)$_3$ fragments to the energy barrier of the reaction, we perform single-point calculations for each fragment at the geometry it has within the full complex for SM, TS1, and TS2, at the B3LYP-
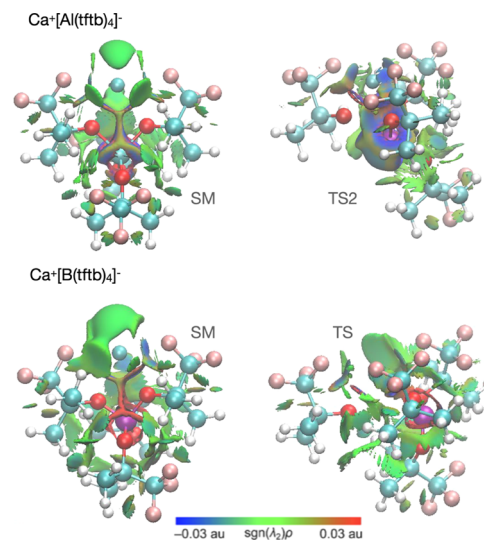
**Figure 7.** NCI plot of the Ca$^+$[Al(tftb)$_4$]$^-$ and Ca$^+$[B(tftb)$_4$]$^-$ complexes.

D3(BJ)[30−32]/def2-TZVPPD[47,48]/CPCM[49] level of theory. Different total charges were imposed for the fragments in the SM and TS to account for the charge separation, e.g., for the CaOR fragment, a total charge of 0 was used for the SM configuration, whereas a total charge of +1 was used for the TS configuration. The fragment-only barrier is then the difference between the fragment energy in its TS configuration and the fragment energy in its SM configuration (eqs (1) and (2)). We also computed the binding energies of these fragments in the SM and TS geometries. For example, the SM binding energy is the difference between the full-complex energy and the sum of the fragment energies in their SM configurations. The difference between the binding energies for the TS and SM geometries is a binding energy barrier (eqs (3)).

$$\Delta E\ddagger(\text{CaOR}) = E([\text{CaOR}]^+ \text{ at TS geom}) \\ - E([\text{CaOR}]^0 \text{ at SM geom}) \quad (1)$$

$$\Delta E\ddagger(\text{Al(OR)}_3) = E([\text{Al(OR)}_3]^- \text{at TS geom}) \\ - E([\text{Al(OR)}_3]^0 \text{ at SM geom}) \quad (2)$$

$$\Delta E\ddagger(\text{binding}) = (E(\text{TS}) - E([\text{CaOR}]^+ \text{at TS geom}) \\ - E([\text{Al(OR)}_3]^- \text{at TS geom})) - (E(\text{SM}) \\ - E([\text{CaOR}]^0 \text{at SM geom}) \\ - E(([\text{Al(OR)}_3]^0 \text{at SM geom})) \quad (3)$$

We plot these energies, as well as the fragment-only barriers in the first two diagrams in Figure 6c. Since the rate-limiting
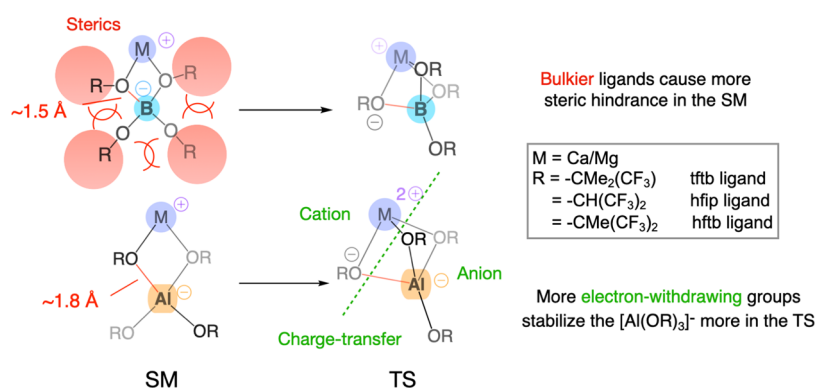
Figure 8. Speculative scheme for the kinetic control of the decomposition pathways (Al–O/B–O bond breakage).

TS is different for $Ca^+[Al(tftb)_4]^-$, $Ca^+[Al(hfip)_4]^-$, and $Ca^+[Al(hftb)_4]^-$, it is important to consider both TS1 and TS2 in the analysis. We observe from Figure 6c that the total electronic energy barrier calculated from both TS1 and TS2 is distinctly higher for $Ca^+[Al(tftb)_4]^-$ than that for $Ca^+[Al(hfip)_4]^-$ and $Ca^+[Al(hftb)_4]^-$. The same trend is found for the fragment-only electronic energy barriers for the $[Al(OR)_3]^0$(SM geom.) → $[Al(OR)_3]^-$(TS geom.) transition (green bars in Figure 6c(1) and (2)), while the corresponding data for the CaOR fragment is roughly constant for the ligand series. Hence, we suggest that the $Al(OR)_3$ fragment effectively determines the barriers and that there exists a significant ligand effect for stabilizing the $[Al(OR)_3]^-$ fragment. The more electron-withdrawing ligands (hfip and hftb) exhibit lower barriers, consistent with the expected anion-stabilizing effects of such groups.

We performed analogous fragment-based calculations on the three borates (see Figure S48); however, in this case, the fragments of the SM and TS configurations were assigned neutral charges to reflect the low amount of charge separation in the full-complex TSs. Similar to the aluminate case, the $B(OR)_3$ fragment-only barriers roughly correlate with the overall barriers, but not with the electron-withdrawing nature of the ligands. This is unsurprising given that the fragments in the calculations are neutral.

Therefore, the charge transfer analysis does not explain the high barrier of the hfip anion within the borate family. To move forward, we note that the hfip ligand possesses a single H atom in the alkoxy group, while the other two borate anions have a methyl group there, which increases the steric hindrance. To quantify the interligand steric repulsions, we divided the SM and TS structures into the core and ligand substructures (Figure 6a) and analyzed the electronic barrier for each component, similar to the above procedure for the CaOR and $Al(OR)_3$ fragments. Each broken covalent bond was compensated with H atoms, whose positions were optimized while holding the other atoms fixed.

We find that the resulting ligand barriers correlate well with the actual barriers (green bars in Figure 6c(3)), and the ligand barrier differences between $Ca^+[B(hfip)_4]^-$ and the other two salts explain ~50% of the actual barrier differences. Furthermore, importantly, we observe that the barrier of the ligand-only subsystem of $Ca^+[B(hfip)_4]^-$ is significantly different from those for $Ca^+[B(tftb)_4]^-$ and $Ca^+[B(hftb)_4]^-$, indicating a distinction in the interligand interactions in the hfip complex. We used the second-generation absolutely localized molecular orbital energy decomposition analysis

(ALMO-EDA2)[50−52] technique to further analyze the various energy components of the interactions between the four bare ligands. The EDA analysis divides the fragment interaction energy into frozen, polarization, and charge transfer contributions. The frozen part can be further divided into several other physically relevant terms, i.e., electrostatics, Pauli repulsion, and dispersion, either through the "classical" or "orthogonal" approaches,[51] where the Pauli repulsion is the term that corresponds most naturally to the concept of steric repulsion. Indeed, we find among the EDA terms, the Pauli repulsion term correlates well with the decomposition barrier for borates: for $Ca^+[B(tftb)_4]^-$ and $Ca^+[B(hftb)_4]^-$, there was an apparent decrease in the Pauli repulsion term going from the SM to TS (−1.44 eV with the classical approach or −0.90 eV with the orthogonal approach for tftb, −1.41 or −0.81 eV for hftb), whereas $Ca^+[B(hfip)_4]^-$ showed a slight increase (0.35 or 0.1 eV). These results support the hypothesis that more steric repulsion exists for the SMs of $Ca^+[B(tftb)_4]^-$ and $Ca^+[B(hftb)_4]^-$, which resolves once one of the ligands dissociates from the tetrahedral geometry and releases the steric strain. We note that the analogous EDA analysis performed on the aluminates did not show any meaningful correlation with the barriers, as the magnitude of all of the EDA components is small (detailed numbers from the EDA analysis are given in SI Section VI).

To summarize our findings, Figure 8 illustrates the origin of the kinetic behaviors of the borate and aluminate salt decomposition pathways through Al–O/B–O bond cleavage. For borate salts, since the B–O bonds are short (~1.5 Å), steric hindrance is significant for bulky ligands confined in the tetrahedral geometry. Comparing the tftb, hfip, and hftb ligands, the hfip ligand is the least bulky; thus, the starting material is less sterically hindered and the highest barrier for breaking the B–O bond is observed. In the case of aluminates where Al–O bonds are longer (~1.8 Å), steric factors are less important and the electronic effects play an essential role in determining the barrier. This is due to the highly charge-transferred nature of the TS (compared to that of the borates), which is stabilized more by functional groups that are more electron-withdrawing. The tftb ligand is the least electron-withdrawing among the three ligands, and therefore the highest barrier is observed.

3. CONCLUSIONS

Motivated by the recent interest in fluorinated alkoxyaluminate/borate electrolytes for multivalent energy storage applications, we performed NMR spectroscopy and an

extensive computational investigation of electrochemical windows and the reductive decomposition pathways through various bond-breaking patterns for a series of fluorinated alkoxyaluminate/borate salts. Kinetic barriers are obtained, for the first time, for the decomposition reactions, which rationalize the reductive behavior and hence electrochemical performance. Across the ligand variations studied, we predict the Al-tftb and B-hfip combinations to be promising candidates based on the calculated high barriers for decomposition through Al/B−O bond breaking under reductive conditions. Our theoretical predictions support previous experimental reports of excellent electrochemical behavior in both Mg and Ca systems for borate salts with hfip ligands. To our knowledge, aluminate salts with tftb ligands have not yet been experimentally studied and investigations are currently underway. We note that changing the solvent component/concentration could affect the solvation structures and thus affect the reaction energies and the barriers in a non-negligible way. As the concentration of CIPs is presumably low with this family of salts due to the weakly coordinating nature of the constituent anions, as is confirmed for $Ca[B(hfip)_4]_2$,[20] the current calculated decomposition barriers may serve as indicators of, e.g., extended cycling, slow decay of the electrolyte.

In addition to the thermodynamic and kinetic results presented here, our mechanistic investigations suggest a significant difference between alkoxyborate and alkoxyaluminate salts in factors controlling the kinetics for Al/B−O bond-breaking decomposition: variations in decomposition barriers for borate salts are mostly determined by steric factors, whereas electronic effects are more important in aluminate salts, suggesting that different design rules should be considered under different scenarios, which will aid in the future design of functional electrolytes.

■ ASSOCIATED CONTENT

Ⓢ Supporting Information

The Supporting Information is available free of charge at https://pubs.acs.org/doi/10.1021/acs.jpcc.2c06653.

Supporting electrochemical windows; decomposition pathways through Al−O/B−O bond breakage; decomposition pathways through C−O bond breakage; decomposition pathways through C−F bond breakage; results from $CaOR-B(OR)_3$ separation for borates; results from EDA analysis; electron affinities for $Al(OR)_3$ and $B(OR)_3$ complexes; spin density plots for structures along the Al/B−O bond breaking decomposition pathways; computational and experimental details; and supplementary NMR spectra (PDF)

xyz files for all of the stationary point structures (ZIP)

■ AUTHOR INFORMATION

Corresponding Author

Kristin A. Persson − *Department of Materials Science and Engineering, University of California, Berkeley, California 94720, United States; Molecular Foundry, Lawrence Berkeley National Laboratory, Berkeley, California 94720, United States;* ⓞ orcid.org/0000-0003-2495-5509; Email: kapersson@lbl.gov.

Authors

Xiaowei Xie − *Department of Chemistry, University of California, Berkeley, California 94720, United States; Materials Science Division, Lawrence Berkeley National Laboratory, Berkeley, California 94720, United States;* ⓞ orcid.org/0000-0001-5618-8768

Noel J. Leon − *Chemical Sciences and Engineering Division, Argonne National Laboratory, Lemont, Illinois 60439, United States*

David W. Small − *Department of Chemistry, University of California, Berkeley, California 94720, United States; Molecular Graphics and Computation Facility, College of Chemistry, University of California, Berkeley, California 94720, United States*

Evan Walter Clark Spotte-Smith − *Materials Science Division, Lawrence Berkeley National Laboratory, Berkeley, California 94720, United States; Department of Materials Science and Engineering, University of California, Berkeley, California 94720, United States;* ⓞ orcid.org/0000-0003-1554-197X

Chen Liao − *Chemical Sciences and Engineering Division, Argonne National Laboratory, Lemont, Illinois 60439, United States;* ⓞ orcid.org/0000-0001-5168-6493

Complete contact information is available at:
https://pubs.acs.org/10.1021/acs.jpcc.2c06653

Notes

The authors declare no competing financial interest.

■ ACKNOWLEDGMENTS

■ REFERENCES

(1) Muldoon, J.; Bucur, C. B.; Gregory, T. Quest for nonaqueous multivalent secondary batteries: magnesium and beyond. *Chem. Rev.* **2014**, *114*, 11683−11720.

(2) Canepa, P.; Sai Gautam, G.; Hannah, D. C.; Malik, R.; Liu, M.; Gallagher, K. G.; Persson, K. A.; Ceder, G. Odyssey of multivalent cathode materials: open questions and future challenges. *Chem. Rev.* **2017**, *117*, 4287−4341.

(3) Tian, Y.; Zeng, G.; Rutt, A.; Shi, T.; Kim, H.; Wang, J.; Koettgen, J.; Sun, Y.; Ouyang, B.; Chen, T.; et al. Promises and challenges of next-generation "Beyond Li-ion" batteries for electric vehicles and grid decarbonization. *Chem. Rev.* **2021**, *121*, 1623−1669.

(4) Elgquist, B.; Wedborg, M. Stability of ion pairs from gypsum solubility degree of ion pair formation between the major constituents of seawater. *Mar. Chem.* **1975**, *3*, 215−225.

(5) Okoshi, M.; Yamada, Y.; Yamada, A.; Nakai, H. Theoretical analysis on de-solvation of lithium, sodium, and magnesium cations to organic electrolyte solvents. *J. Electrochem. Soc.* **2013**, *160*, No. A2160.

(6) Rajput, N. N.; Qu, X.; Sa, N.; Burrell, A. K.; Persson, K. A. The coupling between stability and ion pair formation in magnesium electrolytes from first-principles quantum mechanics and classical molecular dynamics. *J. Am. Chem. Soc.* **2015**, *137*, 3411−3420.

(7) Doe, R. E.; Han, R.; Hwang, J.; Gmitter, A. J.; Shterenberg, I.; Yoo, H. D.; Pour, N.; Aurbach, D. Novel, electrolyte solutions comprising fully inorganic salts with high anodic stability for rechargeable magnesium batteries. *Chem. Commun.* **2014**, *50*, 243−245.

(8) Shterenberg, I.; Salama, M.; Yoo, H. D.; Gofer, Y.; Park, J.-B.; Sun, Y.-K.; Aurbach, D. Evaluation of (CF3SO2) 2N-(TFSI) based electrolyte solutions for Mg batteries. *J. Electrochem. Soc.* **2015**, *162*, No. A7118.

(9) Connell, J. G.; Genorio, B.; Lopes, P. P.; Strmcnik, D.; Stamenkovic, V. R.; Markovic, N. M. Tuning the reversibility of Mg anodes via controlled surface passivation by H2O/Cl-in organic electrolytes. *Chem. Mater.* **2016**, *28*, 8268−8277.

(10) Connell, J. G.; Zorko, M.; Agarwal, G.; Yang, M.; Liao, C.; Assary, R. S.; Strmcnik, D.; Markovic, N. M. Anion Association Strength as a Unifying Descriptor for the Reversibility of Divalent Metal Deposition in Nonaqueous Electrolytes. *ACS Appl. Mater. Interfaces* **2020**, *12*, 36137−36147.

(11) Herb, J. T.; Nist-Lund, C. A.; Arnold, C. B. A fluorinated alkoxyaluminate electrolyte for magnesium-ion batteries. *ACS Energy Lett.* **2016**, *1*, 1227−1232.

(12) Mandai, T.; Youn, Y.; Tateyama, Y. Remarkable electro-chemical and ion-transport characteristics of magnesium-fluorinated alkoxyaluminate−diglyme electrolytes for magnesium batteries. *Mater. Adv.* **2021**, *2*, 6283−6296.

(13) Zhao-Karger, Z.; Bardaji, M. E. G.; Fuhr, O.; Fichtner, M. A new class of non-corrosive, highly efficient electrolytes for rechargeable magnesium batteries. *J. Mater. Chem. A* **2017**, *5*, 10815−10820.

(14) Li, Z.; Fuhr, O.; Fichtner, M.; Zhao-Karger, Z. Towards stable and efficient electrolytes for room-temperature rechargeable calcium batteries. *Energy Environ. Sci.* **2019**, *12*, 3496−3501.

(15) Shyamsunder, A.; Blanc, L. E.; Assoud, A.; Nazar, L. F. Reversible calcium plating and stripping at room temperature using a borate salt. *ACS Energy Lett.* **2019**, *4*, 2271−2276.

(16) Lau, K.-C.; Seguin, T. J.; Carino, E. V.; Hahn, N. T.; Connell, J. G.; Ingram, B. J.; Persson, K. A.; Zavadil, K. R.; Liao, C. Widening electrochemical window of Mg salt by weakly coordinating perfluoroalkoxyaluminate anion for Mg battery electrolyte. *J. Electrochem. Soc.* **2019**, *166*, No. A1510.

(17) Leon, N. J.; Xie, X.; Yang, M.; Driscoll, D. M.; Connell, J. G.; Kim, S.; Seguin, T.; Vaughey, J. T.; Balasubramanian, M.; Persson, K. A.; Liao, C. Room-Temperature Calcium Plating and Stripping Using a Perfluoroalkoxyaluminate Anion Electrolyte. *J. Phys. Chem. C* **2022**, *126*, 13579−13584.

(18) Zhang, Z.; Cui, Z.; Qiao, L.; Guan, J.; Xu, H.; Wang, X.; Hu, P.; Du, H.; Li, S.; Zhou, X.; et al. Novel Design Concepts of Efficient Mg-Ion Electrolytes toward High-Performance Magnesium−Selenium and Magnesium−Sulfur Batteries. *Adv. Energy Mater.* **2017**, *7*, No. 1602055.

(19) Du, A.; Zhang, Z.; Qu, H.; Cui, Z.; Qiao, L.; Wang, L.; Chai, J.; Lu, T.; Dong, S.; Dong, T.; et al. An efficient organic magnesium borate-based electrolyte with non-nucleophilic characteristics for magnesium−sulfur battery. *Energy Environ. Sci.* **2017**, *10*, 2616−2625.

(20) Driscoll, D. M.; Dandu, N. K.; Hahn, N. T.; Seguin, T. J.; Persson, K. A.; Zavadil, K. R.; Curtiss, L. A.; Balasubramanian, M. Rationalizing Calcium Electrodeposition Behavior by Quantifying Ethereal Solvation Effects on Ca2+ Coordination in Well-Dissociated Electrolytes. *J. Electrochem. Soc.* **2020**, *167*, No. 160512.

(21) Hahn, N. T.; Self, J.; Driscoll, D. M.; Dandu, N.; Han, K. S.; Murugesan, V.; Mueller, K. T.; Curtiss, L. A.; Balasubramanian, M.; Persson, K. A.; Zavadil, K. R. Concentration-dependent ion correlations impact the electrochemical behavior of calcium battery electrolytes. *Phys. Chem. Chem. Phys.* **2022**, *24*, 674−686.

(22) Jankowski, P.; Li, Z.; Zhao-Karger, Z.; Diemant, T.; Fichtner, M.; Vegge, T.; Lastra, J. M. G. Development of magnesium borate electrolytes: Explaining the success of Mg[B(hfip)4]2 salt. *Energy Storage Mater.* **2022**, *45*, 1133−1143.

(23) Lu, Z.; Schechter, A.; Moshkovich, M.; Aurbach, D. On the electrochemical behavior of magnesium electrodes in polar aprotic electrolyte solutions. *J. Electroanal. Chem.* **1999**, *466*, 203−217.

(24) Son, S.-B.; Gao, T.; Harvey, S. P.; Steirer, K. X.; Stokes, A.; Norman, A.; Wang, C.; Cresce, A.; Xu, K.; Ban, C. An artificial interphase enables reversible magnesium chemistry in carbonate electrolytes. *Nat. Chem.* **2018**, *10*, 532−539.

(25) Arthur, T. S.; Glans, P.-A.; Singh, N.; Tutusaus, O.; Nie, K.; Liu, Y.-S.; Mizuno, F.; Guo, J.; Alsem, D. H.; Salmon, N. J.; Mohtadi, R. Interfacial insight from operando XAS/TEM for magnesium metal deposition with borohydride electrolytes. *Chem. Mater.* **2017**, *29*, 7183−7188.

(26) Mohtadi, R.; Tutusaus, O.; Arthur, T. S.; Zhao-Karger, Z.; Fichtner, M. The metamorphosis of rechargeable magnesium batteries. *Joule* **2021**, *5*, 581−617.

(27) Zhao-Karger, Z.; Liu, R.; Dai, W.; Li, Z.; Diemant, T.; Vinayan, B.; Bonatto Minella, C.; Yu, X.; Manthiram, A.; Behm, R. J.; et al. Toward highly reversible magnesium−sulfur batteries with efficient and practical Mg [B (hfip) 4] 2 electrolyte. *ACS Energy Lett.* **2018**, *3*, 2005−2013.

(28) Tang, K.; Du, A.; Dong, S.; Cui, Z.; Liu, X.; Lu, C.; Zhao, J.; Zhou, X.; Cui, G. A stable solid electrolyte interphase for magnesium metal anode evolved from a bulky anion lithium salt. *Adv. Mater.* **2020**, *32*, No. 1904987.

(29) Tuerxun, F.; Yamamoto, K.; Mandai, T.; Tateyama, Y.; Nakanishi, K.; Uchiyama, T.; Watanabe, T.; Tamenori, Y.; Kanamura, K.; Uchimoto, Y. Effect of interaction among magnesium ions, anion, and solvent on kinetics of the magnesium deposition process. *J. Phys. Chem. C* **2020**, *124*, 28510−28519.

(30) Becke, A. D. Density-functional thermochemistry. III. The role of exact exchange. *J. Chem. Phys.* **1993**, *98*, No. 5648.

(31) Lee, C.; Yang, W.; Parr, R. G. Development of the Colle-Salvetti correlation-energy formula into a functional of the electron density. *Phys. Rev. B* **1988**, *37*, No. 785.

(32) Grimme, S.; Ehrlich, S.; Goerigk, L. Effect of the damping function in dispersion corrected density functional theory. *J. Comput. Chem.* **2011**, *32*, 1456−1465.

(33) Lin, Y.-S.; Li, G.-D.; Mao, S.-P.; Chai, J.-D. Long-range corrected hybrid density functionals with improved dispersion corrections. *J. Chem. Theory Comput.* **2013**, *9*, 263−272.

(34) Seguin, T. J.; Hahn, N. T.; Zavadil, K. R.; Persson, K. A. Elucidating non-aqueous solvent stability and associated decomposition mechanisms for Mg energy storage applications from first-principles. *Front. Chem.* **2019**, *7*, No. 175.

(35) Lee, H. S.; Yang, X.; Xiang, C.; McBreen, J.; Choi, L. The synthesis of a new family of boron-based anion receptors and the study of their effect on ion pair dissociation and conductivity of lithium salts in nonaqueous solutions. *J. Electrochem. Soc.* **1998**, *145*, No. 2813.

(36) Böhrer, H.; Trapp, N.; Himmel, D.; Schleep, M.; Krossing, I. From unsuccessful H 2-activation with FLPs containing B (Ohfip) 3 to a systematic evaluation of the Lewis acidity of 33 Lewis acids based on fluoride, chloride, hydride and methyl ion affinities. *Dalton Trans.* **2015**, *44*, 7489−7499.

(37) LeBlanc, F. A.; Decken, A.; Cameron, T. S.; Passmore, J.; Rautiainen, J. M.; Whidden, T. K. Synthesis, Characterization, and Properties of Weakly Coordinating Anions Based on tris-Perfluoro-tert-Butoxyborane. *Inorg. Chem.* **2017**, *56*, 974−983.

(38) Mandai, T. Critical issues of fluorinated alkoxyborate-based electrolytes in magnesium battery applications. *ACS Appl. Mater. Interfaces* **2020**, *12*, 39135−39144.

(39) Lapidus, S. H.; Rajput, N. N.; Qu, X.; Chapman, K. W.; Persson, K. A.; Chupas, P. J. Solvation structure and energetics of electrolytes for multivalent energy storage. *Phys. Chem. Chem. Phys.* **2014**, *16*, 21941−21945.

(40) Glendening, E. D.; Landis, C. R.; Weinhold, F. NBO 6.0: Natural bond orbital analysis program. *J. Comput. Chem.* **2013**, *34*, 1429−1437.

(41) Rienstra-Kiracofe, J. C.; Tschumper, G. S.; Schaefer, H. F.; Nandi, S.; Ellison, G. B. Atomic and molecular electron affinities: photoelectron experiments and theoretical computations. *Chem. Rev.* **2002**, *102*, 231−282.

(42) Bader, R. F.; Nguyen-Dang, T.*Adv. Quantum Chem.*; Elsevier, 1981; Vol. *14*, pp 63−124.

(43) Contreras-García, J.; Johnson, E. R.; Keinan, S.; Chaudret, R.; Piquemal, J.-P.; Beratan, D. N.; Yang, W. NCIPLOT: a program for plotting noncovalent interaction regions. *J. Chem. Theory Comput.* **2011**, *7*, 625−632.

(44) Johnson, E. R.; Keinan, S.; Mori-Sánchez, P.; Contreras-García, J.; Cohen, A. J.; Yang, W. Revealing noncovalent interactions. *J. Am. Chem. Soc.* **2010**, *132*, 6498−6506.

(45) Hwang, T.-S.; Wang, Y. Topological Analysis of the Electron Density Distribution of Bis (diiminosuccinonitrilo) nickel, Ni (C4N4H2) 2: Comparison between Experiment and Theory. *J. Phys. Chem. A* **1998**, *102*, 3726−3731.

(46) Popelier, P. L. A.; Aicken, F.; O'Brien, S.*Atoms in Molecules*; Prentice Hall: Manchester, 2000; Vol. *188*.

(47) Weigend, F.; Ahlrichs, R. Balanced basis sets of split valence, triple zeta valence and quadruple zeta valence quality for H to Rn: Design and assessment of accuracy. *Phys. Chem. Chem. Phys.* **2005**, *7*, 3297−3305.

(48) Rappoport, D.; Furche, F. Property-optimized Gaussian basis sets for molecular response calculations. *J. Chem. Phys.* **2010**, *133*, No. 134105.

(49) Barone, V.; Cossi, M. Quantum calculation of molecular energies and energy gradients in solution by a conductor solvent model. *J. Phys. Chem. A* **1998**, *102*, 1995−2001.

(50) Horn, P. R.; Head-Gordon, M. Polarization contributions to intermolecular interactions revisited with fragment electric-field response functions. *J. Chem. Phys.* **2015**, *143*, No. 114111.

(51) Horn, P. R.; Mao, Y.; Head-Gordon, M. Defining the contributions of permanent electrostatics, Pauli repulsion, and dispersion in density functional theory calculations of intermolecular interaction energies. *J. Chem. Phys.* **2016**, *144*, No. 114107.

(52) Horn, P. R.; Mao, Y.; Head-Gordon, M. Probing non-covalent interactions with a second generation energy decomposition analysis using absolutely localized molecular orbitals. *Phys. Chem. Chem. Phys.* **2016**, *18*, 23067−23079.

🗏 Recommended by ACS